Two-dimensional Pitted Corrosion Localization on Coated Steel Based on Fiber Bragg Grating Sensors

Ying Huang [1]*, Fodan Deng [1], Luyang Xu [1], and Fardad Azarmi [2]

[1] Dept. of Civil and Environmental Engineering, North Dakota State University, Fargo, United States, 58108-6050, U.S.A

[2] Dept. of Mechanical Engineering, North Dakota State University, Fargo, United States, 58108-6050, U.S.A

*Corresponding author: ying.huang@ndsu.edu

Abstract Steel is widely used as building material for large-scale structures, such as buildings, bridges, and oil and gas pipelines, due to its high strength-to-weight ratio. Corrosion has been believed to be one of the main reasons for reducing the load carrying capacity and the service life of structural steel, especially for the structures in harsh service environments. To mitigate corrosion for structural steel, coatings have been widely applied. On the other hand, to monitor corrosion in real time, embedding fiber Bragg grating (FBG) inside the coatings becomes a potential solution for coated steel structures. However, due to the fact that FBG sensors are local point sensors, the localization of pitted corrosion based on these sensors are very challenging. In this study, a methodology based on a three-sensor network was set up to detect the location and severity of the pitted corrosion on steel structures in two-dimension (2D). The 2D simply-supported plate theory together with the numerical simulation based on finite element analysis (ANSYS software) was used to derive the transfer function of the pitted corrosion location to the FBG sensor reading. Depending on the parametric study through numerical analysis, a pitted corrosion location exhaustion algorithm was successfully programmed. To verify the feasibility of this algorithm, laboratory experiments were carried out using a steel pipe with three FBG sensors and a temperature compensation sensor embedded inside a layer of epoxy coating (Duralco 4461). The experimental results indicated that the proposed methodology can locate and assess the pitted corrosion on steel structures effectively.

Keywords: Fiber Bragg Grating (FBG); steel; pitted corrosion monitoring; finite element model (FEM); algorithm

1. Introduction

With the rapid development of the construction industry, the durability and integrity of various structures have attracted public attention. Due to its high strength-to-weight ratio, structural steel has been widely used as building material for large-scale structures including buildings, bridges, and oil and gas pipelines. However, structural steel has a drawback compared to other construction materials, concrete or composite materials, which is their vulnerability to corrosion [1-6]. The corrosion of steel is an electrochemical process, which happens naturally when structure steel meets with water and oxygen concurrently. Although there are various factors controlling the process of corrosion, including the physical and chemical properties of steel, the roughness of surface, temperature, etc., it is clear that presence of both water and oxygen is necessary for electrochemical reaction of corrosion to happen. With the presence of free electrons, water and oxygen, reduction happens at cathodes, as shown in the reaction below [2, 6]:

$$2H_2O + O_2 + 4e^- = 4OH^- \tag{1}$$

Reduction reaction at cathodes as shown in Equation (1) introduces a sequence of sub-reactions on steel. When corroded, the iron gets oxidized and then dehydrated to ferrous oxide, ferric oxide and ferro-ferric oxide, resulting in consuming steel as well as producing rust. The produced rust has a volume more than ten times bigger than original iron. Generally, there are two types of corrosion: the general corrosion which is distributed and the pitted corrosion which is localized.

Corrosion, either general or pitted, had been long recognized as one of the main reasons of structural steel component degradation due to its ability to substantially lower the cross-section area of component, causing a substantial deterioration in load-carrying capability of associated structure [7, 8], especially for those in harsh service environments [9]. Steel corrosion has been accounted for big financial loss related to steel structures [10, 11], which was believed to be equivalent to $2.4 trillion globally each year, which makes up 3.4% of the global Gross Domestic Product (GDP) [7, 8]. Although the understanding of corrosion mechanisms and the corrosion detection techniques have been improved, industrial survey reports still show that corrosion plays an important role in structural degradation and safety [12]. For example, as an essential media for transporting oil and gas in the industry through long distances [13], the steel pipelines are vulnerable to corrosion because of the aggressive internal fluids and external environmental conditions, which possibly resulting in leakage and damage [14-17].

To mitigate the corrosion on steel structures, coatings are widely applied to isolate the structural steel from the direct contact of water and oxygen [1, 2, 18], including soft and hard coatings [19-21]. The coatings, which serve as barriers between the steel and outer corrosive environmental, had shown magnificent performance in corrosion mitigation. However, coatings may still fail under certain conditions such as external impacts, abrasions, biology attacks, water scouring, etc. When the coatings failed, usually, the failure of coatings is localized since the external impacts are localized, and the underlying structure would be exposed to corrosive environmental and subjected to pitted corrosion attacks. The corrosion area for coated steel usually is small but very serious. In addition, since it is difficult to be observed or diagnosed during the initial pitted corrosion, and when the corrosion becomes visible, the structural functional degradation may have been severe, and it may be too late to take maintenance measures [22]. Thus, even for coating-protected structures, to ensure the proper functionality of coatings and monitor corrosion for structural steel, detection techniques for pitted corrosion at early stage are needed to verify the performance of coatings and the steel substrate as well as to predict service life [23, 24].

There are several traditional methods used for corrosion detection and assessment, such as weight loss measurement, electromagnetic approach, and non-destructive testing. The first two are destructive assessments. Weight loss measurement, which is also known as exposure test, is simple in concept which measures the weight difference of a coupon (sample) between a certain time interval while placing it in a controlled corrosive environment. The corrosion rate is the weight difference divided by the time elapsed because the weight loss on coupon is exactly the amount of metal consumed by the corrosion reaction. Weight loss measurement is the earliest attempt to perform quantitative corrosion assessment [25, 26], and is also the direct approach to accurately measure the corrosion rate in a certain environment. With statistical study and visual inspection efforts, weight loss measurement could provide additional information such as common early signs for corrosion initialization and corrosion types to guide local corrosion mitigation strategies [27]. However, weight loss measurement is extremely time-consuming and generally takes 30 days to decades to complete depends on the coupons and environment setups. In the excessively long-term weight loss measurement, there also could be problem that at the time measurement was done, the environment to be simulated had already changed while performing the measurement. More importantly, the weight loss approach is not applicable for most soft coating coated steel structures with potential pitted corrosion.

Electrochemical measurement, or electrochemical impedance spectroscopy (EIS), is another destructive method, which was first used in corrosion assessment in 1950s, and fast gained popularity due to its capability of completing measurements in a short period of time while providing and repeatable and reliable results [28-30]. Since the corrosion reaction is one type of electrochemical reaction composing of anode, cathode, and electrolyte, the corrosion rate could be determined by an equilibrium between electrochemical reactions at anode side and cathode side. However, electrochemical techniques are not suitable for large scale steel structures such as bridges or pipelines, and it is not applicable for measuring pitted corrosion for coated structures with soft coatings. In addition, it may induce accelerated corrosion in tested structures.

For large steel structures, several non-destructive corrosion assessment methods have been investigated to evaluate corrosion severity including ultrasonic and acoustic tools and embedded or attached sensors. Ultrasonic measurement methods are one of the most popular corrosion assessment methods used for large steel structures. It provides of high sensitivity, accurate, and immediate assessment for thickness of steel components [31-33]. Similar to all other waves, ultrasound echoes when transmit from one medium to another. Thus, if there is no change in the thickness, the intervals of ultrasonic echoes would be a static value. When corrosion occurs, the steel is consumed, and the thickness is reduced, which could be detected by the ultrasonic wave as the intervals of echoes would change corresponding to the change of thickness. Traditional ultrasonic measurement methods are point-by-point measurement in natural, as it requires ultrasonic wave perpendicularly penetrate the steel, but researches had shown potential of enlarging measurement range when combined with guided wave methods [34, 35]. Ultrasonic measurements showed potential for detecting pitted corrosion in coated steel structures. However, the ultrasonic measurement methods are having difficulties perform assessment on irregular shape parts, and the extensive knowledge requirement for operating and understanding the instrument often limits its application. Furthermore, the ultrasonic measurement requiring human operation on-site could hardly become a candidate for real-time monitoring system of large area.

Acoustic emission (AE) has been widely used for damage monitoring in loaded structures, and researches is trying to adapt it in corrosion assessment and monitoring of steel structures [36, 37]. When there is rapid release of energy within structure, such as the occurrence of a crack, a set of transient elastic waves are generated and transmitted started from that release location. This phenomenon is acoustic emission. By analyzing the properties of AEs transmitted to receiver, the damage could be categorized and localized. AE method as one type of passive detection method is suitable for real-time monitoring and provides high sensitivity, however, it would have low signal-to-noise ratio in field for small cracks, which may not be sensitive enough for detecting pitted corrosion.

Strain sensor-based corrosion assessment methods are gaining attention recently for detecting localized corrosion. When pitted corrosion reactions happen, though original metal is consumed, the corrosion products (oxidized metal) would occupy several times of volume compared with original metal. If the corrosion reaction happens in a confined space, the excessive increased volume would induce a noticeable amount of strain, which could be used as an indicator of corrosion reaction. However, electrical strain gauges may have difficulties applying on steel structures in harsh environments with moisture and intensive electromagnetic noise.

Fiber optic sensors which are made by silica materials have a great potential as a sensing tool in strain-based corrosion assessment of steel structures. Among all fiber optic sensors, fiber Bragg grating (FBG) sensors are well-known for its simplicity in installation, high sensitivity and exceptional durability [38]. An FBG reflects incident lights having a certain wavelength called Bragg wavelength and allows other wavelengths to pass. The Bragg wavelength changes according to the external environmental variation. The FBG has been popularly used to measure strain and temperature [38-40]. A few recent attempts to apply FBG sensors in corrosion monitoring of steel rebar in reinforced concrete and the previous attempt to apply FBG sensors in hard coating in preliminary study had shown the possibility of FBG sensors in corrosion monitoring [41-44]. Relatively low cost of FBG sensors also made large-scale application practical and thus made FBG sensors strong candidate in corrosion monitoring system [45-50]. FBG strain hoop sensor [51] and FBG sensors embedded in coatings by the authors' research group were also investigated to detect pipeline corrosion [52, 53].

Although the FBG has potential to detect pitted corrosion for coated steel structures locally, an FBG sensor is still a localized point sensor which can only perform point measurements to detect the corrosion occurred right on top of the sensor. Thus, if the corrosion does not occur exactly at the locations of the installed sensors, or near the sensors, the effectiveness of the corrosion assessment is questionable. In practical applications, it is very difficult ensure the sensor is installed exactly at the corrosion locations, which limits the wide application of the FBG sensors for corrosion monitoring of steel structures in real time. In this paper, to overcome this challenge, a two-dimensional (2D) sensor network using FBG sensors as well as a location identification theoretic algorithm has been developed to detect the corrosion locations in addition to the corrosion severity for coated steel. The theoretic algorithm has been systematically analyzed through numerical analysis using ANSYS on the proposed 2D corrosion location identification system in addition to laboratory validation experiments. The laboratory validation experiments on a coated steel pipe sample showed that the developed 2D FBG sensor network can simultaneously identify the corrosion location and severity for coated steel effectively.

2. 2D Corrosion localization algorithm

2.1 Plate theory for two-dimensional (2D) corrosion localization

For coated steel, the FBG sensors are assumed to be installed inside the coating to monitor the corrosion occurrence. When pitted corrosion occurs under coatings (either hard or soft coatings), corrosion product (rust) will be produced, whose volume is more than ten times larger than the original steel. Thus, based on the features of a typical pitted or localized corrosion, two reasonable assumptions are made [54]:

1) Since the corrosion is a pitted (localized) corrosion, the product of corrosion is accumulated within a relatively small area comparing to the coating, all the other areas are still perfectly bonded to the substrate;
2) For pitted corrosion, the expansion of corrosion products mainly accumulates vertically.

Based on these assumptions, the expansion induced by the corrosion product compared to original iron can be simulated as a pressure (p) on a very small area (A) in the pitted corrosion location induced load (F) onto the coating as shown in Figure 1. Thus, the load (F) can be calculated by multiplying the pressure (p) with the small corrosion area (A), which is F=pA. In the practice, it is hard to obtain the exact area of the corrosion for estimating the corrosion induced force. However, due to the fact that the coating is relatively thin compared to the steel substrate, a plate theory can be used to simulate the response of the coating with concentrated load induced from corrosion product at location (x_c, y_c). The FBG sensors embedded inside the coating at a random location (x_s, y_s) will detect strains in the coating at that location, which can be used to analyze the location and quantity of the corrosion induced load, F. Thus, in theory, as shown in Figure 1, the corrosion is then simplified as a concentrated force (F) applied at a single point, and the corresponding displacement has its maximum value at the corrosion point and gradually decreases along the way to the edge of the coating surface to zero. However, during the application of the algorithm, subarea will be used to understand the effect of the corrosion area.

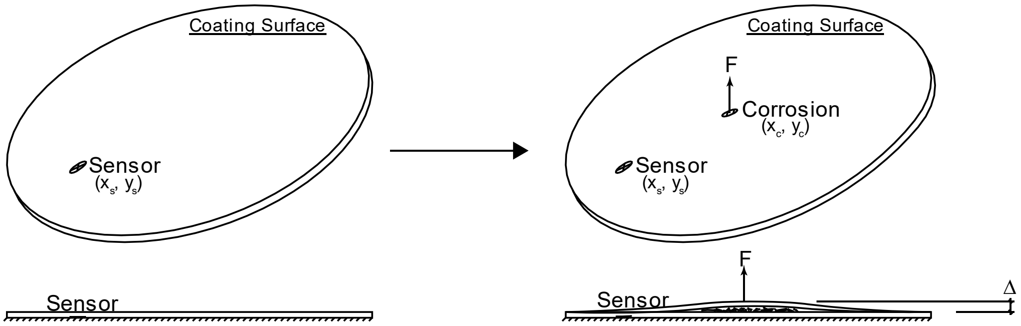

Fig. 1 The dimension of the corrosion plate theory.

Assuming that the coating with known material property (such as Young's modulus, E, and Poisson's ratio, ρ,) and thickness (h) was installed on a steel substrate with known material property and thickness, as the actual boundary condition and the concentrated force F are not explicitly known and the strain at the sensor location has only one exact solution, the strain value at the sensor location could be implicitly given as:

$$\varepsilon_s = f(x_c, y_c, r, F, E, \rho, h, x_s, y_s) \tag{2}$$

where r is the radius of the influenced substrate, E is the Young's modulus, ρ is the Poisson's ratio, h is the coating thickness, (x_c, y_c) is the corrosion location and (x_s, y_s) is the sensor location. From Equation (2), it can be seen that for the same corrosion location and severity, the induced strain quantity depends on the material properties of coating (with dependence on the types of the coating, either polymeric or metal coatings) and the thickness of the coating applied on the surface of the steel. Specifically, the corrosion induced strain will be larger with smaller elasticity of the coating material and thinner thickness of the coating. For polymeric coating, the elasticity of the material is small, but the thickness is usually large. On the other hand, for the metal coatings, the elasticity is big, but the thickness is small. Thus, the induced strains from corrosion need to consider a combination effect of both material property and the thickness of the coatings.

The amounts of center wavelength changes from FBG sensors are determined by the amounts of strains from Equation (2) in the coating induced by the corrosion as below [52, 53]:

$$\frac{\Delta\lambda_B}{\lambda_B} = (1-P_e)\cdot\varepsilon_s + [(1-P_e)\cdot\alpha + \xi]\cdot\Delta T \tag{3}$$

where, P_e is the photoelastic constant of the fiber, α is the thermal expansion coefficient of the fiber, and ξ is a temperature related constant, which can all be determined by the material property of the optical fiber of the FBG sensor. From Equation (3), it can be seen that the center wavelength changes of an FBG sensor can be affected by both strain (ε_s) and temperature changes (ΔT). If a temperature compensation reference sensor is selected with $\lambda_{\mathrm{ref}} \approx \lambda_{\mathrm{B}}$ and installed at the same location, the center wavelength changes for the corrosion induced strains after elimination of temperature effects ($\Delta\lambda = \Delta\lambda_{\mathrm{B}} - \Delta\lambda_{\mathrm{ref}}$) can be expressed as:

$$\Delta\lambda = \Delta\lambda_B - \Delta\lambda_{ref} = (1-P_e)\cdot\lambda_B\cdot\varepsilon_s \tag{4}$$

Based on Equation (2), after the system is designed, the material property, the boundary condition, and the sensor embedded location stay unchanged and can be considered as constants. Thus, it does not matter what types of coatings are applied to embed the sensor as long as the material properties (such as Young's modulus, E, and Poisson's ratio, ρ) and the thickness (h) of the coatings can be known. If a temperature reference sensor can be installed nearby, with the measured center wavelength changes from the FBG sensors, based on (4), the strains at the FBG sensor locations can be detected. Thus, in Equation (2), only the (x_c, y_c) and F which represent the location and the severity of corrosion are unknown and Equation (2) can then be simplified as:

$$\varepsilon_s = f(x_c, y_c, F) \tag{5}$$

Based on Equation (5), if only one sensor was embedded in the system, because the number of unknown parameters had exceeded the number of equations, it could detect the initiation of corrosion, but not the location and the severity of corrosion simultaneously. Therefore, to get both the information of corrosion location and severity beneath the coating, with three unknowns, a minimum of three sensors are needed, as shown in Figure 2. With three sensors in the coating, Equation (5) can then be written as:

$$\begin{aligned} \varepsilon_{s1} &= f_1(x_{sc1}, y_{sc1}, F) \\ \varepsilon_{s2} &= f_2(x_{sc2}, y_{sc2}, F) \\ \varepsilon_{s3} &= f_1(x_{sc3}, y_{sc3}, F) \end{aligned} \tag{6}$$

where ε_{s1}, ε_{s2}, and ε_{s3} represent the measured strains at three sensor locations of Sensor1, Sensor 2, and Sensor 3, respectively; (x_{sc1}, y_{sc1}), (x_{sc2}, y_{sc2}), and (x_{sc3}, y_{sc3}) represent the relative locations between the corrosion and each sensor. To derive the transfer function, Equation (4), a numerical analysis using the finite element model (FEM) is needed because an analytical solution would be very complicated and time-consuming.

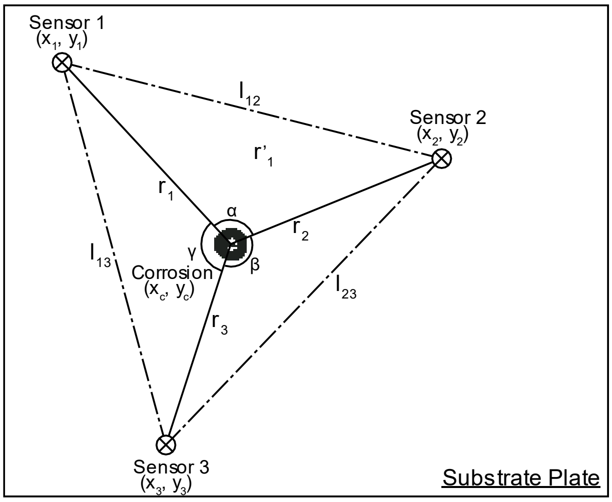

Fig. 2 A three-sensor network to detect corrosion location and severity.

3. Numerical analysis

3.1 Finite element model setup

The numerical analysis can be performed using the fixed sensor location at the center of the simply supported plate and altering the location and severity of corrosion. However, this approach would be consuming too much time to achieve the precision requirement. Another approach which can be inversely used to get the location and severity of corrosion is to fix the corrosion location as shown in Figure 3 and create a strain distribution. Compared with the altering corrosion location, the approach for strain distribution is more time efficient. Based on Figure 3, a finite element model (FEM) was set up in ANSYS, as seen in Figure 4. Because it was assumed that the coating was not detached from the steel substrate other than the localized corrosion area, the out ring of the simply supported plate was fixed all degree of freedom (DOF) as the boundary condition. The corrosion was simulated as a concentrated force applied at the center of the plate, with an amplitude of 1 N. The x-axis and y-axis were within the plate plane, and the z-axis was perpendicular to the plate plane with the positive value representing a direction point upside in Figure 4. Detailed configurations about the FEM are shown in Table 1.

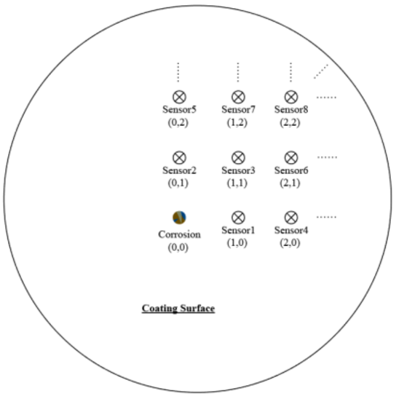

Fig. 3 Simulation model with fixed corrosion location.

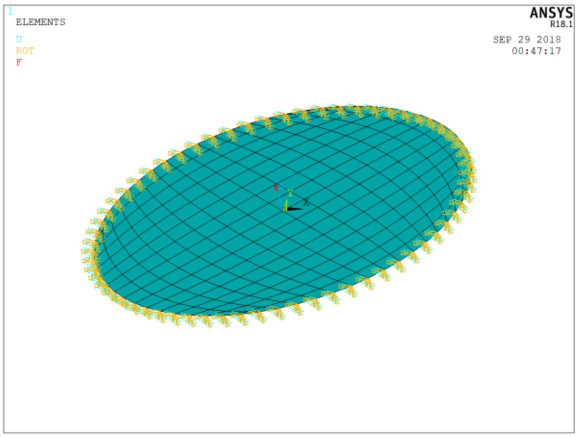

Fig. 4 Circle plate FEM using ANSYS.

Table 1 Configurations of the circle plate FEM.

Unit of length	mm
Unit of force	N
Radius of the plate	10 mm (0.394 in.)
Thickness of the plate	2 mm (0.079 in.)
Young's modulus of the plate	5.157 MPa (748 psi)
Poisson's ratio of the plate	0.29
Element Type	Shell 181

3.2 Numerical analysis results

Figure 5 (a-d) show the simulation results of the circular plate under concentrated load in the middle. Since it was assumed the corrosion initiated at the center, the results showed the maximum strain at the center area. In the distribution of X-direction strain in Figure 5 (a), the gradient of strain along the X-axis was higher than that in Y-axis, as shown in Figure 5 (b). Figure 5 (a, b) also shows that the distributions of X-direction strain and Y-direction strain had a 90-degree difference. Due to the fact that the FBG sensors can only measure strains in their longitudinal directions, the difference between the strain distribution of X-direction and Y-direction suggested that the installation direction of FBG sensors should be carefully designed and recorded. The distribution of the all directional strain intensity and Z-direction displacement were similar as shown in Figure 5 (c, d).

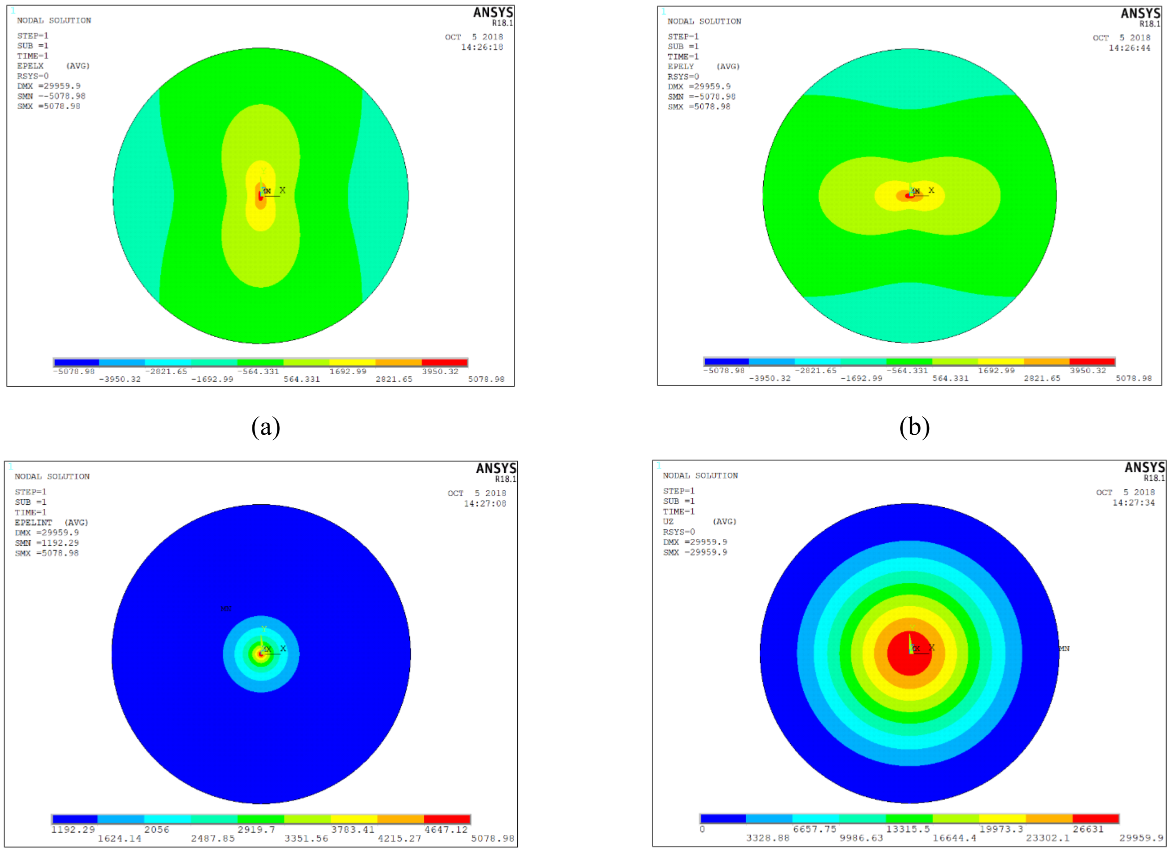

(a) (b)

(c) (d)

Fig. 5 Simulation results of the circular plate model (a) X-direction strain, (b) Y-direction strain, (c) strain intensity, and (d) Z-direction displacement.

In practice, since the coating might not form an exact circle under corrosion attacks, a non-uniform distributed coating bonding strength or defects may result in irregular edge for the circle plate, which was simulated as shown in Figure 6. There were 6 partial circular defects at the edge of the original circle plate model, and their radius were 0.05mm, 0.08mm, 0.06mm, 0.12mm, 0.12mm, and 0.06mm, respectively. Other modeling data of this irregular-edge plate model were the same as shown in Table 1.

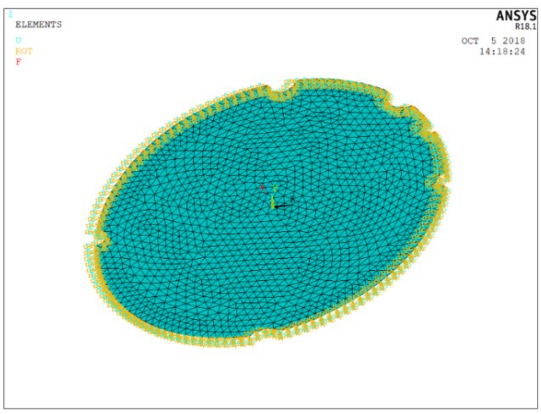

Fig. 6 Simulation model of the irregular edge circular plate.

The distributions of X-axis and Y-axis strains in the center area of the irregular edge circle plate were similar to the circle plate as shown in Figure 7 (a, b), and the only differences were at the edge. Thus, although the coating bonding strength varies, the results from the circle plate may still locate corrosion successfully. Other than that, the strain intensity had a 10% difference compared with the circle plate, and the corrosion severity may not be over-estimated or under-estimated for different bonding conditions, as shown in Figure 7 (c, d).

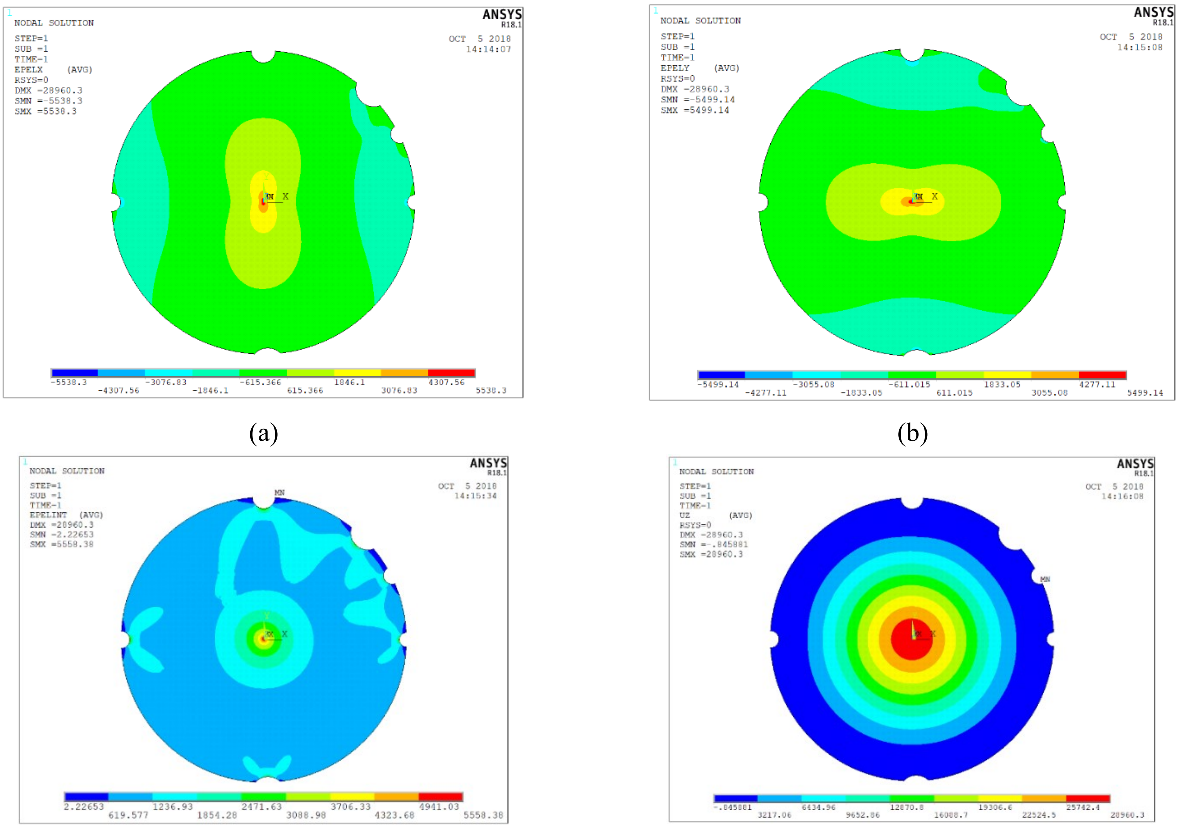

Fig. 7 Simulation results of the irregular edge circle plate model (a) X-direction strain, (b) Y-direction strain, (c) strain intensity, (d) Z-direction displacement.

To search for the possible differences in strain distributions among shapes, rectangular and elliptical coating plates were also simulated, as shown in Figures 8 and 9. The dimension configurations of these two models were shown in Table 2, and other configurations were kept the same as in Table 1.

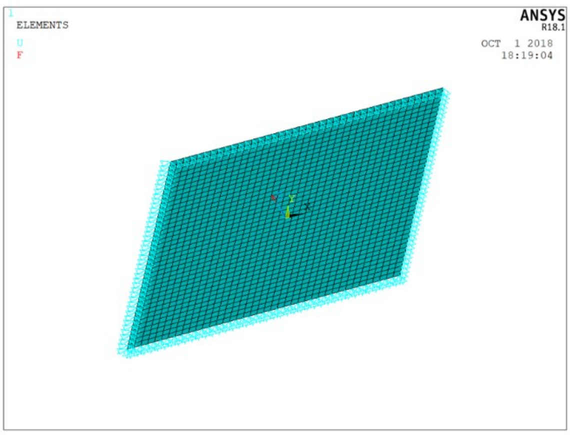

Fig. 8 Simulation model of the rectangular plate.

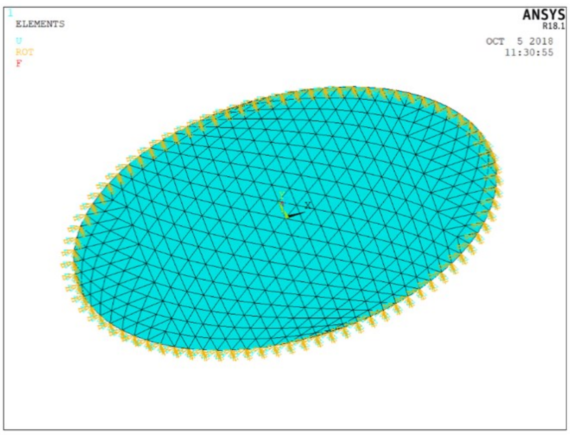

Fig. 9 Simulation model of the elliptical plate.

Table 2 Configurations of the rectangular and elliptical plate models.

Side length of rectangular plate model	10 mm (0.394 in.)
Semi-major axis length of the ellipse plate model	10 mm (0.394 in.)

Semi-minor axis length of the ellipse plate model	8 mm (0.315 in.)

The strain distributions of these two models were similar to those of the circular plate, which each had 90-degree differences between the X-direction strain and the Y-direction strain, as shown in Figures 10 and 11.

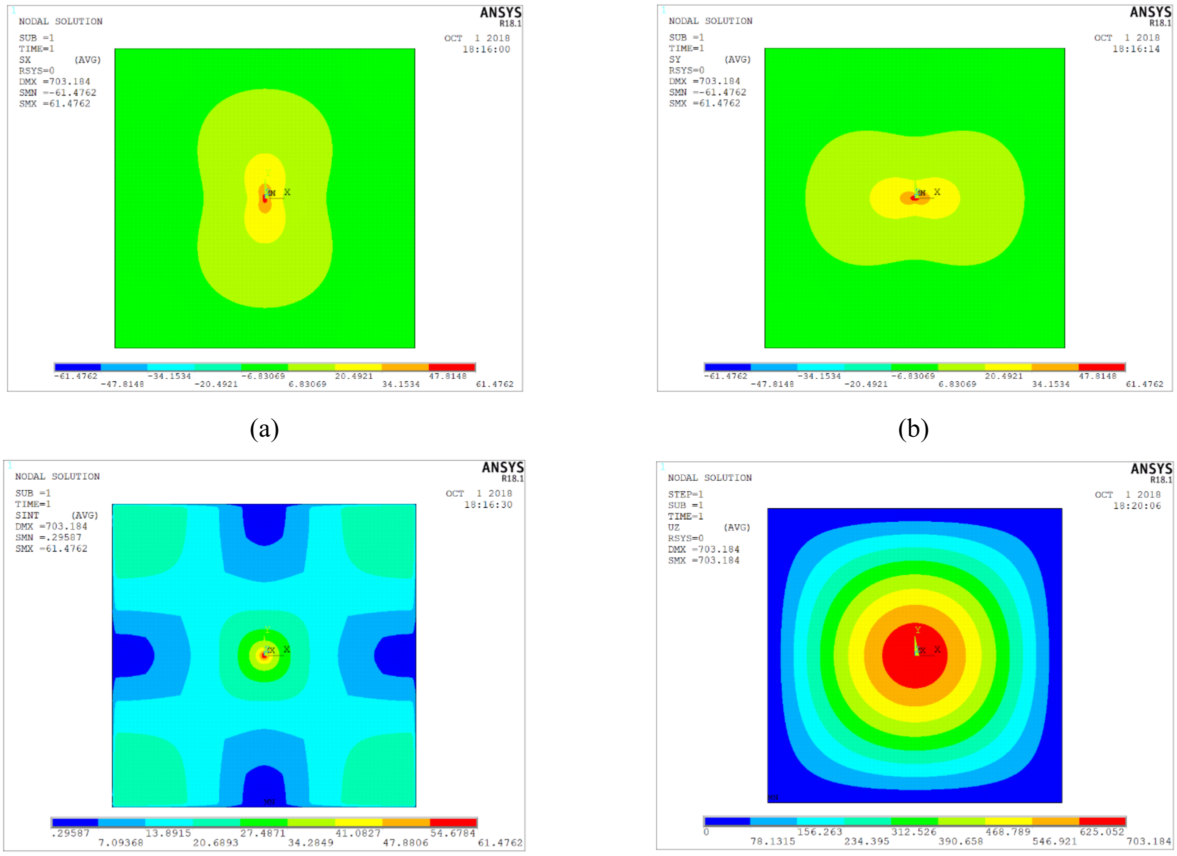

(a) (b)

(c) (d)

Fig. 10 Simulation results of the rectangular plate model (a) X-direction strain, (b) Y-direction strain, (c) strain intensity, (d) Z-direction displacement.

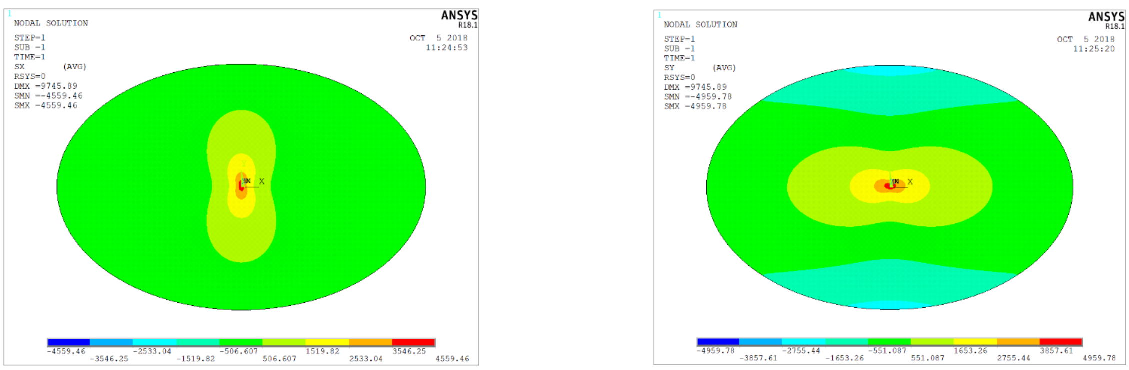

(a) (b)

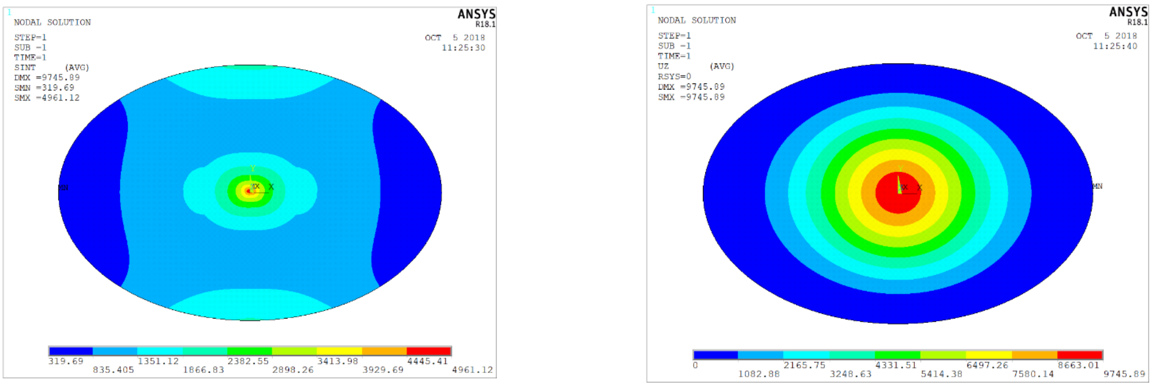

(c) (d)

Fig. 11 Simulation results of the elliptical plate model (a) X-direction strain, (b) Y-direction strain, (c) strain intensity, (d) Z-direction displacement.

3.3 Corrosion localization algorithm

The above four simulated cases covered different boundary conditions and shapes of the proposed plate theories. In all cases, the maximum strain values appeared at the center of the plates, and the distributions were symmetric to the X-axis and Y-axis, suggesting that the installation of FBG sensors should avoid symmetric locations in order to achieve the detection of corrosion location. Even though the strain values in the four cases were different, the strain distributions could be used for the detection of corrosion location. In addition, the use of exhaustion method to solve the transfer function (Equation (4)) to locate the corrosion, we needed a minimum of three sensors, which must follow the same transfer function, using the same severity input and different relative location inputs. Before the corrosion initiated, sensors would have similar readings close to 0. Once the corrosion had initiated, these three sensors would have three different readings since the corrosion induced various strains at different locations, which were noted as ε_1, ε_2, and ε_3 measured from Sensor 1, 2, and 3, respectively. Since the corrosion severity was linear to the strain induced by corrosion, Equation (6) can be re-written as:

$$\begin{aligned} \varepsilon_1 &= S \cdot f_c(x_{sc1}, y_{sc1}) \\ \varepsilon_2 &= S \cdot f_c(x_{sc2}, y_{sc2}) \\ \varepsilon_3 &= S \cdot f_c(x_{sc3}, y_{sc3}) \end{aligned} \tag{7}$$

where f_c is the transfer function for corrosion c; (x_{sc1}, y_{sc1}), (x_{sc2}, y_{sc2}), and (x_{sc3}, y_{sc3}) are the relative locations for three different sensors in regarding to corrosion c; and S is the linear corrosion severity factor.

Since the sensor's locations were fixed after installation, for any possible initiated corrosion (x_c, y_c) with severity factor of 1.0, the strains at the three sensor locations could be calculated as:

$$\begin{aligned} \widehat{\varepsilon_1} &= 1.0 \cdot f_{(x_c, y_c)}(x'_{sc1}, y'_{sc1}) \\ \widehat{\varepsilon_2} &= 1.0 \cdot f_{(x_c, y_c)}(x'_{sc2}, y'_{sc2}) \\ \widehat{\varepsilon_3} &= 1.0 \cdot f_{(x_c, y_c)}(x'_{sc3}, y'_{sc3}) \end{aligned} \tag{8}$$

As a result, if the strains for every possible corrosion location in the sensing area could be calculated, and find a match as:

$$\begin{aligned} \widehat{\varepsilon_1}/\widehat{\varepsilon_3} &= \frac{f_{(x_c, y_c)}(x'_{sc1}, y'_{sc1})}{f_{(x_c, y_c)}(x'_{sc3}, y'_{sc3})} = \frac{S \cdot f_c(x_{sc1}, y_{sc1})}{S \cdot f_c(x_{sc3}, y_{sc3})} = \varepsilon_1/\varepsilon_3 \\ \widehat{\varepsilon_2}/\widehat{\varepsilon_3} &= \frac{f_{(x_c, y_c)}(x'_{sc2}, y'_{sc2})}{f_{(x_c, y_c)}(x'_{sc3}, y'_{sc3})} = \frac{S \cdot f_c(x_{sc2}, y_{sc2})}{S \cdot f_c(x_{sc3}, y_{sc3})} = \varepsilon_2/\varepsilon_3 \end{aligned} \tag{9}$$

Then, the corrosion location c could be estimated at (x_c, y_c). And the linear corrosion severity factor could be calculated as:

$$S = \varepsilon_1/\widehat{\varepsilon_1} \tag{10}$$

Then, if the sensing area can be divided into several subareas that were described using Euclidean space for every sensor and every possible initiated corrosion, their locations could be demonstrated using the subareas that contained them. The corrosion severity factor, S, can be estimated for each subarea and the location of the corrosion can be estimated accordingly. The determination of the size of the subarea depends on several factors, including the size of the FBG sensors (usually 2~2.5 mm, around 0.1 in.), the expected corrosion area size of the pitted corrosion based on experiences, the required corrosion detection accuracy, and the available computational capacity and computational efficiency needed. Since the FBG sensors usually have a size of 2.5~5 mm (0.1~0.2 in.) and the pitted corrosion also ranges from the size of several millimeters (several 0.04 in.) in diameter, the minimum size of a square subarea needs to be larger than the size of a FBG sensor, which is 2.5~5 mm (0.1~0.2 in.) in each side. If the computational capacity and efficiency is allowed, the size of 2.5 mm (0.1 in.) is suggested for the subarea.

To illustrate how this algorithm working, a specific example was given to a steel plate which can be divided into a four by seven (4×7) subareas as shown in Figure 12 with the locations of Sensor 1, Sensor 2, and Sensor 3 placing in the subareas of (3, 4), (4, 1), and (6, 2), and the assumed possible corrosion initiating at subarea (3, 2). The square subarea used the suggested minimum size of 2.5 mm (0.1 in.) in each side. Then, the measured strains of these three sensors for this initiated corrosion can be given as:

$$\begin{aligned} \varepsilon_1 &= S \cdot f_c(0,2) \\ \varepsilon_2 &= S \cdot f_c(1,-1) \\ \varepsilon_3 &= S \cdot f_c(3,0) \end{aligned} \tag{11}$$

As the computer program tried to exhaust all possible corrosion locations, it would start at the first possible corrosion location $(1,1)$, and the calculation results would be:

$$\begin{aligned} \widehat{\varepsilon_1} &= 1.0 \cdot f_c(2,3) \\ \widehat{\varepsilon_2} &= 1.0 \cdot f_c(3,0) \\ \widehat{\varepsilon_3} &= 1.0 \cdot f_c(5,1) \end{aligned} \tag{12}$$

The results of Equation (10) would not match the proportional relationship in Equation (7). So, the detection algorithm of exhaustion corrosion location would move on to the next possible corrosion location $(2,1)$, and calculated again, as shown in Figure 13.

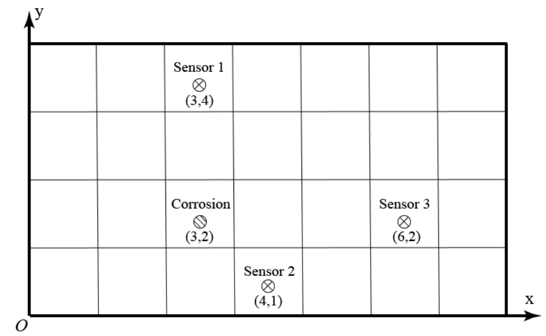

Fig. 12 An example for exhaustion method in the detection of corrosion location.

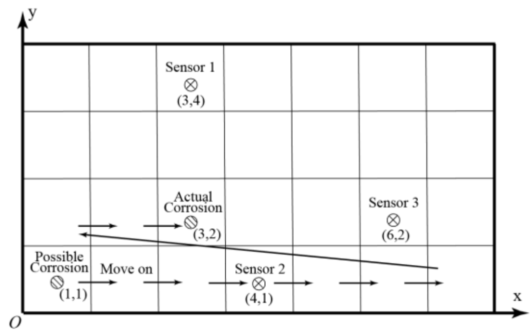

Fig. 13 Iterative exhaustion method in the detection of corrosion location.

Until it reached the assuming possible corrosion location $(3,2)$, the calculated results would be:

$$\begin{aligned} \widehat{\varepsilon_1} &= 1.0 \cdot f_c(0,2) \\ \widehat{\varepsilon_2} &= 1.0 \cdot f_c(1,-1) \\ \widehat{\varepsilon_3} &= 1.0 \cdot f_c(3,0) \end{aligned} \tag{13}$$

The results finally matched the actual sensors' readings, as shown below:

$$\widehat{\varepsilon_1}/\widehat{\varepsilon_3} = \frac{1.0 \cdot f_c(0\,,2)}{1.0 \cdot f_c(3\,,0)} = \frac{f_c(0\,,2)}{f_c(3\,,0)} = \frac{S \cdot f_c(0\,,2)}{S \cdot f_c(3,0)} = \varepsilon_1/\varepsilon_3 \tag{14}$$

$$\widehat{\varepsilon_2}/\widehat{\varepsilon_3} = \frac{1.0 \cdot f_c(1\,,-1)}{1.0 \cdot f_c(3\,,0)} = \frac{f_c(1\,,-1)}{f_c(3\,,0)} = \frac{S \cdot f_c(1\,,-1)}{S \cdot f_c(3\,,0)} = \varepsilon_2/\varepsilon_3$$

Thus, the corrosion location had been detected successfully at the current location $(3, 2)$.

For higher precision requirement of detecting corrosion location, the sensing area needs be divided into a greater number of and smaller subareas. In this case, the computing power requirement might increase dramatically as the number of subareas increases. To solve this possible limitation in computing power, the theoretical strains at sensors' locations for every possible initiated corrosion location could be calculated once and stored. Thus, when the corrosion detection system was running, instead of exhausting the whole sensing area for every single strain reading of sensors, to achieve to detect the corrosion location only requires the comparisons between the monitored strain value ratios and stored strain value ratios, which could save huge amount of time.

4. Laboratory experiments and result analysis

4.1 Experimental setup and results

To validate the developed corrosion localization algorithm, a laboratory experiment was conducted using one steel pipe which was coated with a layer of epoxy soft coating (Duralco 4461). Although epoxy was used in the laboratory validation tests, the developed algorithm can be used for any types of coatings as long as the material properties of the coatings can be known. The steel pipe for laboratory testing was selected to represent an irregular surface of steel instead of regular flat plate. The steel pipe is NPS size 6 schedule 40 pipe with A36 structural steel, a diameter of 168.275mm (6.625 in.), a thickness of 7.112mm (0.28 in.) and a length of 250mm (10 in.). Although the lab tests used the outer surface of steel pipe as an example, the sensors do not need to be restricted on the outside of the pipes, and the tested pipe is only an example for validation in the lab, it can be inside as well. In practical applications of steel pipes, if buried underground, the corrosion damages on external surfaces normally are initialized by external damages such as cracks, dent, or peal of coating materials. These mechanical damages usually are formed during installation construction process with rocks in soil hitting the external surface of the pipes and damage the coatings, or the damages can also be formed because of nearby excavation working along the buried pipes without knowing the locations of the pipes. Excavation has caused more than 50% of the external damages on coatings of buried pipes and it happens very frequently. As long as a crack, peal, or dent on the coating materials occurs, the corrosion will quickly initialize and progress to reduce the thickness of the pipe since it is directly in contact with wet soil. In addition, it worth mentioning that the developed algorithm can be applied to any steel structures whose coatings can be applied to embed the sensors accordingly, such as steel bridges or buildings. Since the steel pipes have curved surfaces which are much more difficult shapes to be monitored compared with flat surfaces, the steel pipes were used as examples in this study. Three FBG sensors and a temperature compensation FBG sensor were embedded inside the epoxy coating. All the four FBG sensors have the same initial center wavelength of 1540.00nm and the same length of 5mm (0.2 in.). Sensor 1 is 10mm (0.4 in.) away from Sensor 3 in the diameter direction and Sensor 2 is 20mm (0.8 in.) away from Sensor 1 in the longitudinal direction of the steel pipe as shown in Figure 14. To ensure a secured bonding between the FBG sensors and the subsurface, the FBG sensors were firstly attached to the external surface of the steel pipe at the designed locations as shown in Figure 14 (a) using epoxy carefully before the application of the general coating.

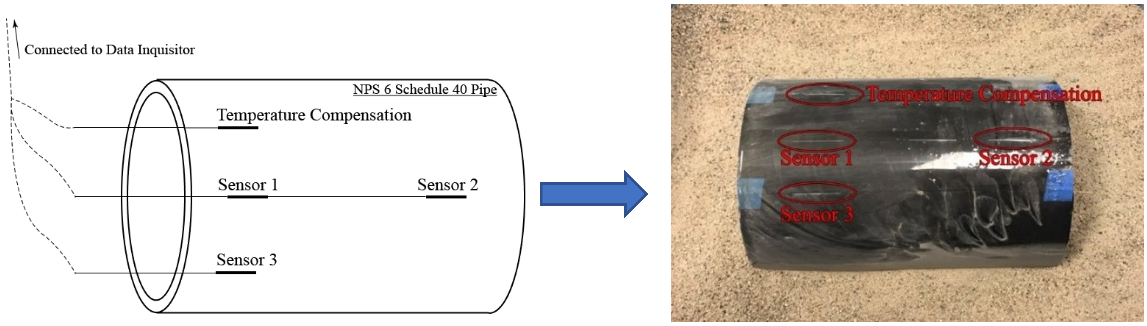

(a) (b)

Fig. 14 Sensor layout (a) and steel pipe sample for detection of corrosion location (b).

The steel pipe sample was buried in moisture sand after the soft coating was fully cured, and 3.5wt% NaCl solution was sprayed on to the sand every other day to maintain a corrosive environment around the sample. The center wavelength changes of the embedded FBG sensors had been recorded using optical signal analyzer (National Instruments PXIe-4844 Optical Sensor Interrogator integrated with PXIe-1071 Controller and PXIe-8133 Chassis) continuously during the entire experiment. It has four optical channels that are simultaneously sampled at 10 Hz for measurement of all the four embedded FBG strain and temperature sensors. The integrator has a wavelength measurement accuracy of 1pm and measurement range between 1510nm to 1590nm. The experimental setup was shown in Figures 15 (a, b).

(a) (b)

Fig. 15 Experimental setup (a) and buried sample in sand (b)

The experiment ran for a total of 60 days. On the 31st day, a small crack was made intentionally near Sensor 1 on the coating to simulate a damage on the coating for the corrosion location and to accelerate the corrosion initiation because the deterioration rate of the soft coating was slow, and the corrosion might not initiate before the damage of the soft coating. The corrosion simulated crack location was near Sensor 1 as shown in Figure 16. The measured Bragg wavelength changes of the three sensors were shown in Figure 17, and the crack time was marked in the graph. It can be seen that the center wavelengths of Sensor 1 and Sensor 3 increased for a short time before they dramatically dropped after the crack was made because the coating delamination was caused by the aggressively expanding corrosion progress. From Figure 17, a four-stage process has been observed for the corrosion of coated steel using epoxy. At Stage 1, the made crack resulted in coating delamination. The delamination of the coating would release the strains on the coating and induce a reduction in strains on the coating. This reduction of strains would introduce a decrease of center wavelength of the FBG sensors nearby, which was clearly indicated by the trends of the FBG center wavelength changes as Stage 1 in Figure 17. However, as the expansion of the corrosion, the delamination of the corrosion would be stable and stop after a while since the corrosion product would restrict the air reaching the inner surface beneath the coating. Thus, after a couple of days, the delamination would be saturated and the boundary condition of the pitted corrosion became stable, resulting in Stage 2. In Stage 2, the corrosion product then would be accumulated in the vertical direction of the coating, resulting in the re-increase of the strains on the coating and the increase of the center wavelength of the embedded FBG sensors as clearly shown as Stage 2 in Figure 17. In Stage 3, the crack would grow because of the accumulation of the corrosion product and delaminate the coating to release the strains. In Stage 4, the corrosion was stabilized since the air was not so easy to reach the uncorroded steel and would maintain steady for very long time before further increase of corrosion. However, the Bragg wavelength of Sensor 2 did not change much (within 5 pm) during the entire experiment, which indicates that the corrosion initiated far away from Sensor 2.

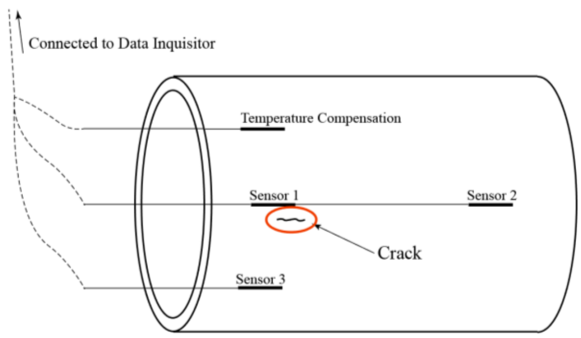

Fig. 16 Crack location of the coating on the steel pipe.

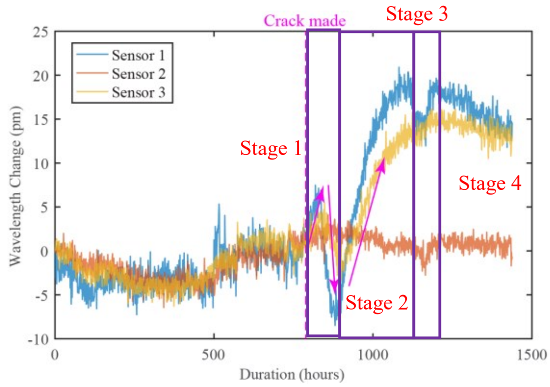

Fig. 17 Bragg wavelength change vs time.

4.2 Corrosion location identification using developed algorithm

The transfer function used in the experiment was simulated using FEM analysis and the result was shown in Figure 18. The entire sensing area was set as half of the steel pipe surface, and the sensing area was divided into 10,000 subareas with 100 rows and 100 columns as seen in Figure 19. The subarea size of each unit used the minimum size of 2.5mm (0.1 in.) and all sensor locations used the mid-points of the Bragg gratings. The locations of Sensor 1, 2, and 3 were (15, 50), (85, 50), and (15, 18), respectively. The crack intentionally made was at (15, 45).

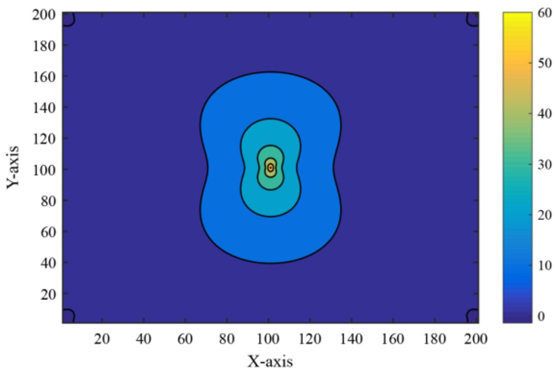

Fig. 18 The strain map induced by corrosion.

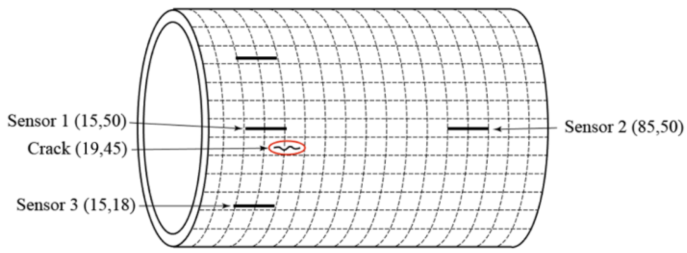

Fig. 19 Definition of steel pipe subareas.

Because there was no corrosion before the crack was made to the soft coating, the Bragg wavelength changes of all three sensors were close to zero, and the strain ratios ($\varepsilon_1/\varepsilon_3$ and $\varepsilon_2/\varepsilon_3$) were unstable. As a result, the proposed algorithm cannot match any corrosion location during this period. After the crack was intentionally made to the soft coating, the corrosion started to occur. However, the corrosion caused a coating crack in a short time before the Bragg wavelength change curve had a stable increase. The strain values of Sensor 1 and Sensor 3 were close to zero, so the proposed algorithm was not able to match any location in the first increase of the Bragg wavelength change curve. After the Bragg wavelength change curve dropped due to the delamination of the soft coating, the corrosion location was successfully detected during the second increase of the Bragg wavelength change curve, as shown in the highlighted and framed part of Figure 20. It was clearly observed that the Sensor 1 and Sensor 3 had larger center wavelength changes compared to the Sensor 2, and the strain ratio ($\varepsilon_1/\varepsilon_3$) was stable.

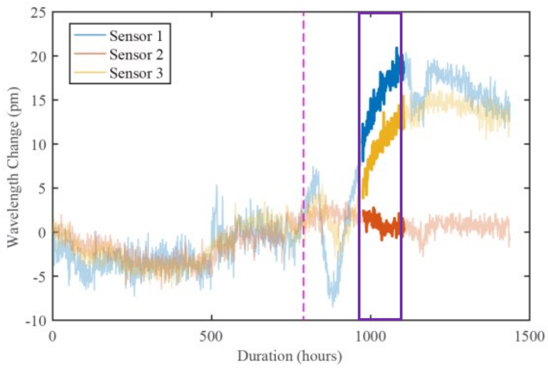

Fig. 20 The Bragg wavelength change curve with highlighted successful detection of corrosion location.

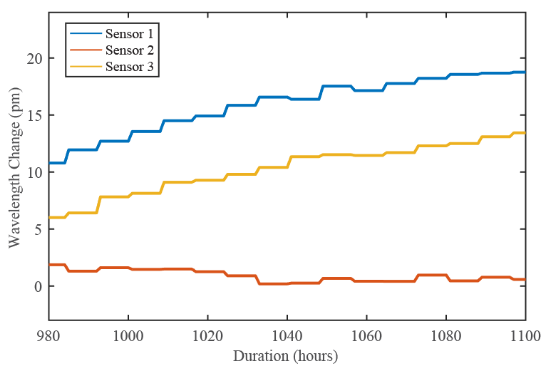

Fig. 21 Zoomed denoised inputs of the Bragg wavelength change curve.

To avoid the influence from the changes of the boundary condition changes, the corrosion localization algorithm was applied after the boundary condition was stable and a part of the Stage 2 as framed in Figure 20. The Bragg wavelength changes as framed in Figure 20 was denoised using wavelet package in MATLAB before the algorithm was applied. The denoised highlighted part of the date was shown in Fig. 21. The strain inputs were divided into three segments and the average strain ratio values for each segment were served as inputs in the algorithm of corrosion detection, as shown in Fig. 22. For the first, second, and third segments (Segment 1, Segment 2, and Segment 3), corrosions located by the algorithm were at (25, 32), (17, 42), and (23, 47). From the crack location and the visual inspection result as shown in Fig. 23, the actual corrosion location was at (19, 45), which was 1.3 inches, 0.4 inches, and 0.4 inches away from estimations of Segment 1, Segment 2, and Segment 3, respectively. The estimation results of the algorithm suggested that the corrosion location detected from Segment 2 and Segment 3 were more accurate compared to Segment 1. It could be predicted that this algorithm is more accurate when the corrosion was at a stable increase stage.

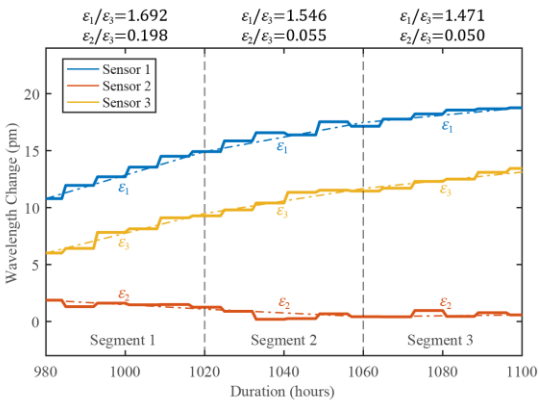

Fig. 22 Three segments and the strain ratios of the Bragg wavelength change curve.

Fig. 23 Visual inspection result of the steel pipe sample on the 60th day.

5. Conclusion

In this study, a novel 2D corrosion localization algorithm for coated steel structures based on embedded FBG sensors was developed. The simply supported plate theory was used to locate two-dimensional corrosion. Through conducting numerically and experimentally comprehensive investigations, specific conclusions could be drawn from this study as follow:

1) The two-dimensional (2D) simply supported plate theory can be applied to identify the corrosion locations using a sensor network with a minimum of three embedded FBG sensors in the coating;
2) The developed two-dimensional (2D) simply supported plate model can analyze the transfer function between the corrosion locations and the corrosion severity to locate it using FEM analysis;

3) By using the method of exhaustion, the algorithm of corrosion location was successfully programmed. With the numerical solution of the transfer function from the finite element model, the mothed of exhaustion can be used as the algorithm to estimate corrosion locations and corrosion severity when Bragg wavelength change curves were interrogated from embedded FBG sensors.
4) The proof-of-algorithm laboratory experimental results indicated that the proposed assessment system of corrosion could identify the corrosion locations effectively within 12mm (0.5 inches).

The developed method is preferred to have the sensors embedded inside coatings, thus, it may be more applicable for new structures which would have coatings applied during construction. However, since the coatings for any existing structures may require recoating as the coatings will be wearied away as time goes. So the sensors can also be embedded during the re-coating or repair process. It is also worth mentioning that flat steel surfaces in steel buildings and bridges are easier to be accessed compared with existing buried steel pipes and so if existing steel structures are the targeted structures, the developed technique may be more applicable for existing steel buildings and bridges. In addition, further advance will be made to validate the algorithm for different damage severities and locations, and multiple corrosions occurring at the sensing area, which requires a sensor network with more than three sensors embedded and an updated estimation algorithm for corrosion locations. Also, more analysis on the size of corrosion area (subarea) will be needed for expanding the developed algorithm for practical applications. More importantly, there was no field application using the proposed system. Thus, it is of interest to be applied to an actual steel structure for field testing, which hopefully can be done in the near future.

Acknowledgment

This work was supported by the National Science Foundation under the agreement of No. 1750316.

References

1. R. Pierre, Handbook of corrosion engineering. McGraw-Hill Professional, 1999.
2. M. Fontana and N. Greene, Corrosion Engineering, 3rd Edition. McGraw-Hill book Company, 1987.
3. A. Estrada-Vargas, N. Casillas, S. Gomez-Salazar, and M. Barcena-Soto, "Corrosion of aluminum, copper, brass and stainless steel 304 in tequila," International Journal of Electrochemical Science, Vol. 7, pp. 7877–7887, 2012.
4. U. Evans, "The Corrosion and Oxidation of Metals: Scientific Principles and Practical Applications, 1960," London: Edward Arnold, p. 324.
5. R. E. Melchers and R. Jeffrey, "Early corrosion of mild steel in seawater," Corrosion Science, Vol. 47, pp. 1678–1693, 2005.
6. C. Southwell, J. Bultman, and A. Alexander, "Corrosion of metals in tropical environments. Final report of 16-year exposures," Materials Performance (MP), Vol. 15, 1976.
7. C. E. Balestra, M. G. Lima, A. R. Silva, and R. Medeiros-Junior, "Corrosion degree effect on nominal and effective strengths of naturally corroded reinforcement," Journal of Materials in Civil Engineering, Vol. 28, pp.04016103 2016.
8. W. Li, T. Liu, J. Wang, D. Zou, and S. Gao, "Finite-element analysis of an electromechanical impedance–based corrosion sensor with experimental verification," Journal of Aerospace Engineering, Vol. 32, 04019012, 2019.
9. Z. Li, Z. Jin, T. Zhao, and P Wang, "Use of a novel electro-magnetic apparatus to monitor corrosion of reinforced bar in concrete," Sensors, Vol. 286, pp. 14-27, 2019.
10. L. Jin, R. Zhang, X. Du, and Y. Li, "Investigation on the cracking behavior of concrete cover induced by corner located rebar corrosion," Engineering Failure Analysis, Vol. 52, pp. 129-143, 2015.
11. R. A. De Medeiros-Junior, M. G. De Lima, P. C. De Brito, and M. De Medeiros, "Chloride penetration into concrete in an offshore platform-analysis of exposure conditions," Ocean Engineering, Vol. 103, pp. 78-87, 2015.
12. O. Shabarchin, and S. Tesfamariam, "Internal corrosion hazard assessment of oil & gas pipelines using Bayesian

belief network model," Journal of Loss Prevention in the Process Industries, Vol. 40, pp. 479-495, 2016.
13. L. Ren, T. Jiang, Z. Jia, D. Li, C. Yuan, and H. Li, "Pipeline corrosion and leakage monitoring based on the distributed optical fiber sensing technology," Measurement, Vol. 122, pp.57-65, 2018.
14. Jiang, T., Ren, L., Jia, Z., Li, D. & Li, H. J. A. S. Application of FBG based sensor in pipeline safety monitoring. 7, 540 (2017).
15. L. Evers, L. Ceranna, H. W. Haak, A. Le Pichon, and R. Whitaker, "A seismoacoustic analysis of the gas-pipeline explosion near Ghislenghien in Belgium," Bulletin of Seismological Society of America, Vol. 97, pp. 417-425, 2007.
16. S. Shin, "Risk-based underground pipeline safety management considering corrosion effect," Journal of Hazardous Materials, Vol. 342, pp. 279-289, 2018.
17. F. Richards, "Failure Analysis of a natural gas pipeline rupture," Journal of Failure and Prevention, Vol. 13, pp. 653-657, 2013.
18. W. K. Muhlbauer, Pipeline risk management manual: ideas, techniques, and resources. Gulf Professional Publishing, 2004.
19. A. Weishaar, A. "Evaluation of self-healing epoxy coatings for steel reinforcement," Construction and Building Materials, Vol. 191, pp. 125-135, 2018.
20. A. Tiwari, "A topical review on hybrid quasi-ceramic coatings for corrosion protection," Corrosion Reviews, Vol. 36, pp. 117-125, 2018.
21. S. M. Hassani-Gangaraj, A. Moridi, and M. Guagliano, "Critical review of corrosion protection by cold spray coatings," Journal of Surface Engineering, Vol. 31, pp. 803-815, 2015.
22. A. Ranjith, K. B. Rao, and K. Manjunath, "Evaluating the effect of corrosion on service life prediction of RC structures–A parametric study," International Journal of Sustainable Built Environment, Vol. 5, pp. 587-603, 2016.
23. C. H. Tan, F. R. M. Adikan, Y. G. Shee, B. K. Yap, "Non-destructive fiber Bragg grating based sensing system: Early corrosion detection for structural health monitoring," Sensors and Actuators A: Physical, Vol. 268, pp. 61-67, 2017.
24. E. Soares, "Structural integrity analysis of pipelines with interacting corrosion defects by multiphysics modeling," Engineering Failure Analysis, Vol. 97, pp. 91-102, 2019.
25. R. Baechler, "Corrosion of metal fastenings in zinc chloride-treated-wood after 20 years," in Proceedings, American Wood Preservers' Association, 1949, vol. 45, pp. 390-397.
26. T. Wright, H. Godard, and I. Jenks, "The Performance of Alcan 65S-T6 Aluminum Alloy Embedded in Certain Woods Under Marine Conditions," Corrosion, Vol. 13, No. 7, pp. 77-83, 1957.
27. S. L. Zelinka and D. R. Rammer, Review of test methods used to determine the corrosion rate of metals in contact with treated wood. US Department of Agriculture, Forest Service, Forest Products Laboratory Madison, WI, 2005.
28. F. Mansfeld and S. Tsai, "Laboratory studies of atmospheric corrosion—I. Weight loss and electrochemical measurements," Corrosion Science, Vol. 20, pp. 853–872, 1980.
29. W. Mueller, "Theory of the polarization curve technique for studying corrosion and electrochemical protection," Canadian Journal of Chemistry, Vol. 38, pp. 576–587, 1960.
30. Y. Zou, J. Wang, and Y. Zheng, "Electrochemical techniques for determining corrosion rate of rusted steel in seawater," Corrosion Science, Vol. 53, pp. 208–216, 2011.
31. C. Bescond, S. Kruger, D. Lévesque, R. Lima, and B. Marple, "In-situ simultaneous measurement of thickness, elastic moduli and density of thermal sprayed WC-Co coatings by laser-ultrasonics," Journal of thermal spray technology, Vol. 16, pp. 238–244, 2007.
32. F. Lakestani, J.-F. Coste, and R. Denis, "Application of ultrasonic Rayleigh waves to thickness measurement of metallic coatings," NDT & E International, Vol. 28, pp. 171–178, 1995.

33. G. Rosa, R. Oltra, and M.-H. Nadal, "Evaluation of the coating–substrate adhesion by laser-ultrasonics: Modeling and experiments," Journal of applied physics, Vol. 91, pp. 6744–6753, 2002.
34. W. Zhu, J. Rose, J. Barshinger, and V. Agarwala, "Ultrasonic guided wave NDT for hidden corrosion detection," Journal of Research in Nondestructive Evaluation, Vol. 10, no. 4, pp. 205-225, 1998.
35. J. Sargent, "Corrosion detection in welds and heat-affected zones using ultrasonic Lamb waves," Insight-Non-Destructive Testing and Condition Monitoring, Vol. 48, no. 3, pp. 160-167, 2006.
36. J. Miguel, J. Guilemany, B. Mellor, and Y. Xu, "Acoustic emission study on WC–Co thermal sprayed coatings," Materials Science and Engineering: A, Vol. 352, pp. 55–63, 2003.
37. G. Wang, M. Lee, C. Serratella, and S. Botten, "Testing of acoustic emission technology to detect cracks and corrosion in the marine environment," Journal of Ship Production and Design, Vol. 26, no. 2, pp. 106-110, 2010.
38. E. J. Friebele, "Fiber Bragg grating strain sensors: present and future applications in smart structures," Optics and Photonics News, Vol. 9, p. 33, 1998 1998.
39. P. Moyo, J. Brownjohn, R. Suresh, and S. Tjin, "Development of fiber Bragg grating sensors for monitoring civil infrastructure," Engineering structures, Vol. 27, no. 12, pp. 1828-1834, 2005.
40. D. Betz, W. Staszewski, G. Thursby, and B. Culshaw, "Multi-functional fibre Bragg grating sensors for fatigue crack detection in metallic structures," Proceedings of the Institution of Mechanical Engineers, Part G: Journal of Aerospace Engineering, Vol. 220, pp. 453–461, 2006 2006.
41. A. Maryoto and T. Shimomura, "Numerical Simulation for Corrosion Crack in Concrete Members Considering Penetration of Corrosive Product," Simulation, Vol. 2, 2013 2013.
42. Z. Zheng, X. Sun, and Y. Lei, "Monitoring corrosion of reinforcement in concrete structures via fiber Bragg grating sensors," Frontiers of Mechanical Engineering in China, Vol. 4, pp. 316–319, 2009 2009.
43. P. Biswas, S. Bandyopadhyay, K. Kasavan, S. Parivalla, B. A. Sundaram, K. Ravisankar, K. Dasgupta, "Investigation on packages of fiber Bragg grating for use as embeddable strain sensor in concrete structure," Sensors and Actuators A: Physical, Vol. 157, pp. 77–83, 2010 2010.
44. J. Gao, J. Wu, J. Li, and X. Zhao, "Monitoring of corrosion in reinforced concrete structure using Bragg grating sensing," NDT & E International, Vol. 44, pp. 202–205, 2011 2011.
45. T. Jiang, L. Ren, Z. Jia, D. Li, and H. Li, "Pipeline internal corrosion monitoring based on distributed strain measurement technique," Structural Control and Health Monitoring, Vol. 24, pp. e2016, 2017.
46. Y. Cheng, C. Zhao, J. Zhang, and Z. Wu, "Application of a Novel Long-Gauge Fiber Bragg Grating Sensor for Corrosion Detection via a Two-level Strategy," Sensors, Vol. 19, pp. 954, 2019.
47. L. Fan, Y. Bao, and G. Chen, "Feasibility of distributed fiber optic sensor for corrosion monitoring of steel bars in reinforced concrete," Sensors, Vol. 18, pp. 3722, 2018.
48. C. Tan, Y. Shee, B. K. Yap, F. M. Adikan, "Fiber Bragg grating based sensing system: Early corrosion detection for structural health monitoring," Sensors and Actuators A: Physical, Vol. 246, pp. 123-128, 2016.
49. O. Almubaied, H. K. Chai, M. R. Islam, and K. S. Lim, "Monitoring corrosion process of reinforced concrete structure using FBG strain sensor," IEEE Transction on Instrumentation and Measurement, Vol. 66, pp. 2148-2155, 2017.
50. J. R. Lee, C. Y. Yun, and D. J. Yoon, "A structural corrosion-monitoring sensor based on a pair of prestrained fiber Bragg gratings," Measurement Science and Technology, Vol. 21, p. 017002, 2009.
51. L. Ren, Z. Jia, H. Li, and G. Song, "Design and experimental study on FBG hoop-strain sensor in pipeline monitoring," Optical fiber technology, Vol. 20, pp. 15–23, 2014.
52. F. Deng, Y. Huang, F. Azarmi, and Y. Wang, "Pitted corrosion detection of thermal sprayed metallic coatings using fiber Bragg grating sensors," Coatings, Vol.7, pp. 35, 2017.
53. F. Deng, Y. Huang, and F. Azarmi, "Corrosion behavior evaluation of coated steel using fiber Bragg grating

sensors," Coatings, Vol. 9, pp. 55, 2019.

54. R. E. Melchers, and R. Jeffrey, "Early corrosion of mild steel in seawater," Corrosion Science, Vol. 47, pp. 1678-1693, 2005.